# Characterization of the passive layer on ferrite and austenite phases of super duplex stainless steel

Rahimi, E.; Kosari, Ali; Hosseinpour, S.; Davoodi, Ali; Zandbergen, H.; Mol, Johannes M.C.

**DOI**
10.1016/j.apsusc.2019.143634

**Publication date**
2019

**Document Version**
Accepted author manuscript

**Published in**
Applied Surface Science

# Characterization of the passive layer on ferrite and austenite phases of super duplex stainless steel

**Ehsan Rahimi[a,b,§], Ali Kosari[c,§], Saman Hosseinpour[d,§,*], Ali Davoodi[a,*], Henny Zandbergen[e], Johannes M.C. Mol[c]**

[a] Materials and Metallurgical Engineering Department, Faculty of Engineering, Ferdowsi University of Mashhad, Mashhad 91775-1111, Iran

[b] Department of Engineering and Architecture, University of Udine, 33100 Udine, Italy

[c] Department of Materials Science and Engineering, Delft University of Technology, Mekelweg 2, 2628 CD Delft, The Netherlands

[d] Institute of Particle Technology (LFG), Friedrich-Alexander-Universität-Erlangen-Nürnberg (FAU), Cauerstraße 4, 91058 Erlangen, Germany

[e] Kavli Institute of Nanoscience, Delft University of Technology, Lorentzweg 1, 2628 CJ Delft, The Netherlands

[§] Authors with equal contribution

*Corresponding authors: S. Hosseinpour (saman.hosseinpour@fau.de) & A. Davoodi (a.davodi@um.ac.ir)

## Abstract

In this study, we report on a combined microscopic, analytical and electrochemical characterization of the nanoscopic passive layer on a tungsten-molybdenum-containing super duplex stainless steel. We used scanning transmission electron microscopy/energy dispersive X-ray spectroscopy, scanning Kelvin probe force microscopy, scanning tunneling spectroscopy, and Mott–Schottky electrochemical impedance spectroscopy analysis to correlate the local chemical composition and electronic properties of passive layers on austenite and ferrite phases. The passive layer on the ferrite phase contains a higher amount of Mo, W, and Cr, which accommodates a higher nobility of ferrite and a higher local energy of the band gap compared to those on the austenite. The two aforementioned phases exhibit a different composition and semi-conductive properties of their passive layers leading to dissimilar local corrosion susceptibility. These findings are of pivotal importance in further studies of austenite and ferrite phase resolved corrosion resistance of duplex stainless steel demanding a dedicated alloying strategy.

**Graphical Abstract**

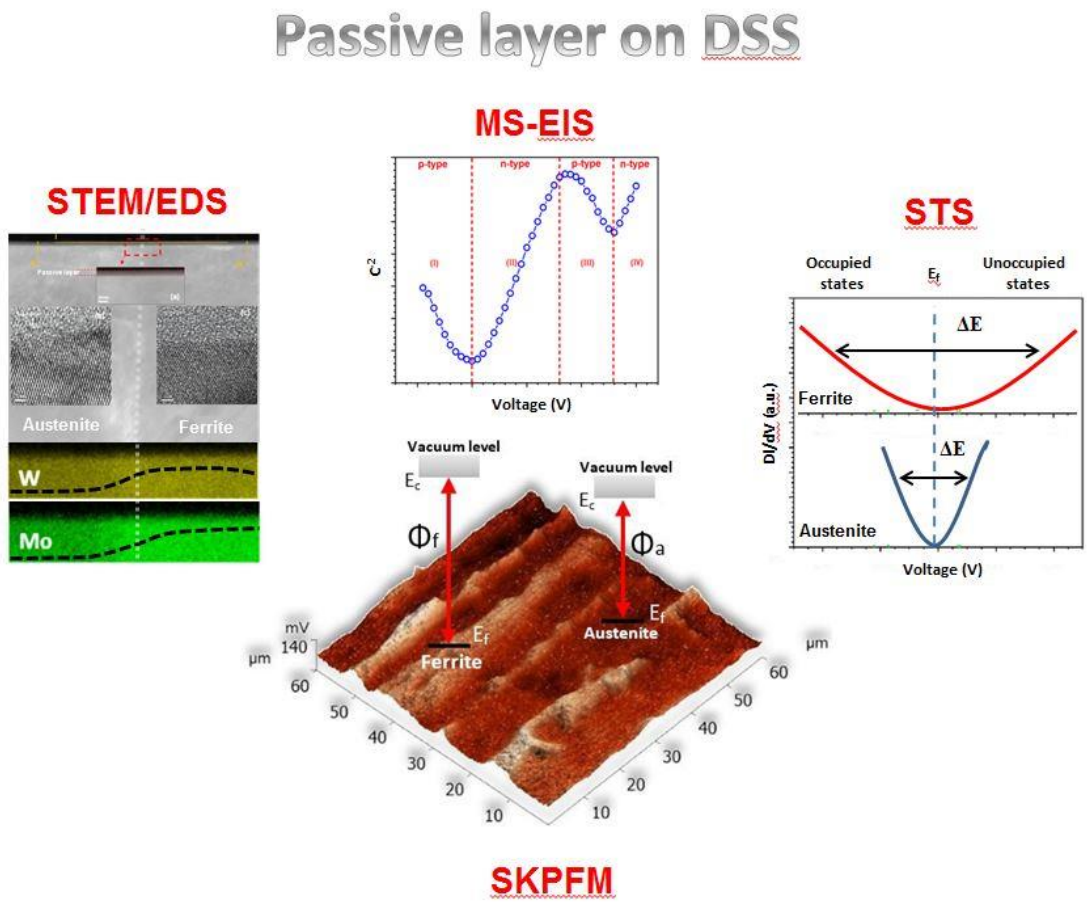


**Highlights**

- The passive layer on ferrite in super DSS contains a higher amount of Mo, W, and Cr compared to that formed on austenite.
- The passive layers on ferrite and austenite in super DSS exhibit different semiconducting properties.
- The passive film on DSS is composed of a p-type inner layer and an n-type outer layer.
- Inner and outer passive layers have different density of defects in their structure.

**Keywords:** A. Stainless steel; B. STEM/EDS; B. SKPFM; B. STS; C. Passive film

## 1. Introduction

The microstructure of duplex stainless steel (DSS), which consists of austenite and ferrite phases in roughly equal proportion, accommodates outstanding mechanical properties as well as generally superior corrosion resistance compared to conventional grades of stainless steel [1, 2]. However, coexistence of austenite and ferrite with alloying elements at dissimilar levels may result in heterogeneous corrosion of DSS in extremely harsh environments. In general, in corrosive environments like chloride-containing solutions, especially at elevated temperature, austenite is more prone to localized corrosion attack (i.e. pitting corrosion) compared to ferrite [3, 4]. Additionally, the austenite phase often shows a higher dissolution rate than ferrite in acidic solutions like $H_2SO_4$ where a galvanic coupling is also expected [5]. This behavior can be linked to the different bulk chemical composition of the two phases, promoting passive layers with different corrosion properties on austenite and ferrite [2, 6].

The high corrosion resistance of DSS is generally attributed to the semi-conductive properties of the surface passive film. In fact, the semi-conductivity of the passive film plays a critical role in the film breakdown process, which is mainly controlled by ionic and electronic mobility processes [7, 8]. The semi-conductive properties of the passive film can be modified by adding alloying elements at different levels to the bulk, although the effect of other factors like solution chemistry and pH, pre-treatment and mechanical history of alloy cannot be ruled out [1]. As is recently reported, compared to chromium and molybdenum, tungsten can provide DSS with a higher passive film stability and re-passivation kinetics [1]. Nevertheless, the extent to which tungsten can contribute to enhancement of the passive layer properties is limited by several factors including economical restrictions and its adverse impacts on mechanical properties of DSS [9]. The enhanced corrosion performance of DSS upon addition of tungsten is correlated to the prevention of anion attack and cation ejection due to the formation of tungsten trioxide ($WO_3$) in the passive film [10]. Furthermore, tungsten anions ($WO_4^{-2}$) are reported to act as an inhibitor in the electrolyte inside pits or crevice [9, 10]. Therefore, it is expected that the passive films on ferrite and austenite phases within DSS exhibit variations in their corrosion resistance, as they comprise tungsten at different level.

For a ternary Fe-Cr-Ni stainless steel, the cross section of passive layer can be divided into inner and outer regions, in terms of chemical composition [1, 3, 11]. Line profile analysis by scanning transmission electron microscopy equipped with energy dispersive X-ray spectroscopy

(STEM/EDS) have revealed nickel accumulation at the inner side of the passive layer (i.e. passive layer/matrix interface) where a chromium depleted-zone is observable. Furthermore, chromium has been detected at higher concentration in the inner region of the passive layer than in the outer region whereas it is opposite for iron [3]. However, in the new generation of super DSS which comprise more alloying elements and coexistence of multiple phases, the microstructure and chemical composition of passive layer on each phase might be more complex than those on simple alloys. Therefore, a combination of different characterization techniques is required to assess the structure, chemical composition, and electronic properties of the passive layer on each phase. A major analytical challenge is to measure the extent and distribution at which minor alloying elements like tungsten and molybdenum incorporate into the oxide layer.

To this point, many works have been devoted to studying the passivity and selective dissolution of different phases in DSS and a variety of techniques have been utilized for characterization of microstructure, chemical composition, electronic properties, as well as corrosion protection properties of passive layer on DSS. For instance, Femina et al. used electrochemical scanning tunneling microscopy (ECSTM) [12] and scanning Auger electron spectroscopy (SAES) [13] to resolve local electrochemical events occurring at the phase/grain boundary regions in different DSSs with various chemical compositions. They found that partitioning of alloying elements, e.g. Mo and Cr in the ferrite phase and Ni and N in the austenite phase, in the higher alloyed DSSs results in homogeneous dissolution of the two phases in DSS, by strengthening the initially weak sites of ferrite adjacent to austenite. They observed such composition gradients across the boundary of the two phases which extends to a few micrometers. Guo et al. [14] used atomic force microscopy (AFM) to determine the local electron work function of phases in DSS and concluded that the different properties of ferrite and austenite in DSS, such as adhesive force or modulus, are intrinsically related to their electron work function. However, caution should be used in the interpretation of local Volta potential results obtained by SKPFM, as the measured values in air are not always correlated with the real corrosion potentials in aqueous solutions [15]. They also used magnetic force microscopy (MFM) [16] to properly identify different phases in electropolished DSS and used current sensing atomic force microscopy (CSAFM) [7] to determine the electrical properties of the passive film on DSS, before and after passivation. Their results indicated that conductivity of the passive layer on both ferrite and austenite phases decreases as the passive film thickens, and correlated this trend to the change of the chemical composition of the passive film as it grows. Scanning electrochemical microscopy

(SECM) was used by de Assis et al. [17] to address the preferential dissolution of ferrite in DSS. Cheng et al. [1], on the other hand, used SECM and observed that the galvanic effect beneficially affects the passivity of the film on both phases in DSS. Jin et al. developed a test system by combining lithography and electrochemical microcapillary cell [18] to acquire local electrochemical properties on DSS with micrometer lateral resolution and proposed that the corroion resistance in DSS decreases in the order austenite > austenite/ferrite interface > ferrite. Örnek et al. [19] and Sathirachinda et al. [20] used scanning Kelvin probe force microscopy (SKPFM) to study the changes of nobility of ferrite and austenite in DSS after different heat treatments. Based on their observations long ageing treatment results in the reduction of the nobility of all phases, with the biggest detrimental impact on ferrite. The effect of annealing and cold rolling on the nobility of phases in DSS [21] and the influence of hydrogen charging on the pitting corrosion of DSS [22] was also studied using SKPFM. It was noted that upon hydrogen charging in DSS, low potential areas emerge mainly at the ferrite/austenite boundary or inside the ferrite phase. These low potential areas are preferential sites for nucleation of pitting corrosion. Yao et al studied the passive film on DSS using photoelectrochemical techniques, angular resolved X-ray photoelectron spectroscopy (AR-XPS), and Mott-Schottky analysis and determined the semiconducting properties of the passive film at different applied potentials in an alkaline borate buffer solution [23]. They identified both n-type and p-type semiconducting characteristics in the passive layer formed at different potentials, pointing toward a double layer structure for the passive film on DSS. In a recent work by Gardin et al. [24] XPS and time of flight secondary ion mass spectroscopy (ToF-SIMS) 3D chemical mapping were coupled to compare the native oxide and electrochemically formed passive film on austenite and ferrite in DSS. They clearly showed that the condition in which the passive layer on DSS is formed affects the distribution of alloying elements in ferrite and austenite phases.

In this work, we utilize a combination of SKPFM, scanning tunneling spectroscopy (STS), STEM/EDS, and Mott-Schottky electrochemical impedance spectroscopy (MS-EIS) to get new insights into the role of alloying elements in the bulk of adjacent ferrite and austenite phases in a super DSS on the chemical composition, nobility, and charge carrier properties of their respective passive layers. For this purpose, S39274 super duplex stainless steel was selected, as this alloy consists of austenite and ferrite phases next to one another, with dissimilar content of alloying elements like chromium, nickel, molybdenum, nitrogen and tungsten. The Volta potential is regarded as a measure of the electrical properties of metal or semi-conductor surfaces, including

oxides or passive films that are formed in air, electrolyte, or under applied potential, and represents the relative nobility of different constituents within heterogeneous materials [19, 25]. In fact, the Volta potential is sensitive to any kind of chemical variations, structural changes, or surface defects and can be used to unravel the electrochemical activities indirectly, especially in prediction of corrosion behavior [15, 19, 26-28]. Complementary STS and MS-EIS analysis allows determining the semiconducting properties of passive layer, whereas STEM/EDS provides information on local microstructure and chemical composition variations in the bulk ferrite and austenite phases as well as their passive layers, yet unreported in prior literature.

## 2. Experimental details

The specimens were cut out of a pipe sheet of UNS S39274 super duplex stainless steel (Nipon steel & Sumitomo metal company) with a thickness of 5 mm and surface area of 1.5 $cm^2$. The chemical composition of S39274 super DSS was measured by a spark atomic emission spectrometer (Spectro M8) according to ASTM E1086 [29], and the nominal composition is provided in Table 1, together with the chemical composition of individual austenite and ferrite phases, which are determined by integrating the elemental line profiles measured by EDS. The samples were wet polished to a mirror-like finish according to ASTM E3-11 [30], using successive grades of SiC papers up to 3000 grit followed by a final polishing step with alumina slurry-impregnated polishing cloth. After polishing, the samples were rinsed with ethanol followed by hot air blow drying. All scanning probe microscopy measurements were performed on the polished specimens, without any prior electrochemical treatments. SKPFM and STS analysis were carried out on samples with a native passive layer, to characterize the relative surface Volta potential distribution and electronic property of ferrite and austenite phases. For this purpose, automatically interchangeable measuring heads were used which were integrated into the Solver Next SPM (AFM-STM) instrument. The relative Volta potential mappings were performed in a dynamic lift-up mode at a scan frequency rate of 0.3 Hz, a pixel resolution of 512 ×512, at 27 ºC and a relative humidity of 28 %. AFM tip during mapping was n-type antimony-doped silicon pyramid single crystal with a conductive PtIr (10 nm) coating and a Cr adhesive layer (2.5 nm). STS measurements were carried out with a sharpened Pt tip by the cut-and-pull technique [31] at about 60º angle with special cutting scissors. The distance between tip and sample was fixed by applying a constant bias voltage of 1 V and a set point current of 0.4 nA. The normalized differential conductance spectra were collected from the tunneling currents in the scanning voltage range of -0.5 V to +0.5

V. In order to achieve better counting statistics, the STS measurements were performed multiple times and the results were averaged on individual ferrite and austenite phases. To enhance the thickness of the passive film on the samples for TEM characterizations, a mirror-like polished bulk sample was immersed in 45% $HNO_3$ solution for 24 h. To detect the passive film thickness and alloying element distribution in both ferrite and austenite phases, TEM analysis in a Titan Cs-corrected 300 kV TEM facility equipped with an EDS detector (Oxford instrument) was performed. The cross-sectional thin specimens were obtained from the grain-boundary regions where both austenite and ferrite phases are included, using a Helios G4 FEI focused ion beam (FIB) and lift-out procedure [32]. For the electrochemical measurements, a Vertex.One.EIS Ivium potentiostat instrument was used with a saturated calomel electrode (SCE, +245 vs. SHE) and a platinum plate as the reference and counter electrodes, respectively. The Mott-Schottky EIS measurements were performed in a 3.5 %wt NaCl solution at 1 to 1000 Hz frequency range in 10 frequency steps and in the potential range of -1 to 1.1 V vs. SCE, with an amplitude value of ±10 mV. Accuracy of the Mott-Schottky EIS analysis was confirmed by modeling the individual EIS spectra at selected potentials, which could be fitted with a constant phase element (CPE) having n close to 1. Prior to the Mott-Schottky EIS measurements, the working electrodes were immersed in the 3.5 %wt NaCl corrosive solution for 1 hour, to enable the steady state open circuit potential (OCP) condition to establish.

**Table 1.** Main alloying elements in UNS S39274 super DSS and in individual ferrite and austenite phases (wt %).

| Element | Ni | Cr | Mo | W | N | Fe and other minor alloying elements |
|---|---|---|---|---|---|---|
| Super DSS | 5.94 | 24.51 | 3.49 | 2.58 | 0.25 | Bal. |
| Ferrite | 3.81 | 27.45 | 4.78 | 2.88 | 0.04 | Bal. |
| Austenite | 7.21 | 24.23 | 3.16 | 1.58 | 0.46 | Bal. |

## 3. Results and discussion

To determine the impact of alloying elements on nobility and semi-conductive properties of ferrite and austenite phases, we obtained SKPFM distribution maps of S39274 super DSS over a 60 × 60 $\mu m^2$ area as shown in Fig. 1a. The lower Volta potential in this map (darker regions) corresponds to the austenite phase whereas the ferrite phase possesses the higher Volta potential values (lighter regions) confirming the observations in Ref. [7, 8]. As listed in Table 1, austenite

and ferrite have different contents of alloying elements. It is obvious that the enrichment of tungsten, chromium, and molybdenum in ferrite phases has a more positive effect on the work functions than enrichment of nickel and nitrogen in the austenite phase [7, 33]. Therefore, according to SKPFM results, ferrite is expected to be more noble than austenite and as such a lower electrochemical activity is expected for the ferrite phase, which is in line with prior works [2-5]. For quantitative analysis, the Volta potential distribution is presented as a histogram in Fig. 1b and it is de-convoluted into two peaks using the multimodal Gaussian distribution analysis, according to Eq. 1 [28]:

$$Y=\frac{1}{\sigma\sqrt{\frac{\pi}{2}}}\exp\left[-\frac{2(x-\mu)^2}{\sigma^2}\right] \quad (1)$$

where $Y$ represents the counts number, $\sigma$ is the standard deviation, and $\mu$ is the mean Volta potential value. Based on the extracted parameters from SKPFM image using histogram analysis the ferrite phase (nobler component) shows a higher mean Volta potential value (~101 mV) as compared to austenite islands (~65 mV). This potential difference between the austenite and ferrite phases ($\Delta V$=36 mV) can explain the occurrence of localized corrosion attacks at grain boundaries toward austenite phase, as was reported in [9, 21]. Additionally, the austenite phase exhibits a higher standard deviation value (std= ~21.0 mV, resulting in a wider peak in Fig. 1b) than ferrite phase (std= ~11.5 mV), which can be attributed to higher compositional heterogeneities within the austenite phase [34], a phenomenon which has recently been observed using high resolution EDS line profile analysis [35]. Nevertheless, a quantitative measure of such heterogeneity can be realized using statistical approaches like histogram analysis, as shown in Fig. 1b. Fig. 1c schematically illustrates the spatial frequency distribution of the measured Volta potentials superimposed on the 3D Volta potential map. Detailed information on Volta potential distribution can be obtained by power spectral density (PSD) analysis of SKPFM data; as shown in Fig. 1d. The PSD plot, calculated by the following equation, correlates the Volta potential components to their spatial distribution [36]:

$$\mathrm{PSD(f)} = \lim_{A\to\infty}\frac{1}{A}\left|\int_A z(r)\exp(-2\pi i f.r)dr\right|^2 \quad (2)$$

where $z(r)$ represents the Volta potential data of the surface area , $A$ is the surface area of the measuring field, $r$ is the position vector, and f is the spatial frequency vector in the $x-y$ plane, as shown in Fig. 1c. Low and high frequency oscillations in this figure schematically demonstrate the

correlation concept of Volta potential and spatial frequencies on ferrite and austenite phases. In the PSD graph (Fig. 1d), the lowest spatial frequencies with high Volta potential are related to ferrite and the highest spatial frequencies with the low Volta potential correspond to austenite phase.

As mentioned earlier, the semi-conductivity is a crucial factor affecting the charge carrier characteristics of the passive layer. To further explore the macroscopic semi-conducting characteristics of passive film on super DSS in contact with a corrosive solution, we performed Mott-Schottky EIS analysis using the following equation [23, 37]:

$$\frac{1}{C_H^2} + \frac{1}{C_{SC}^2} = \pm \frac{2}{\varepsilon \varepsilon_0 e N_{(d\ or\ a)} A^2} \left(E - E_{fb} - \frac{kT}{e}\right) \quad (3)$$

where $C_{SC}$ represents the space charge capacitance, $C_H$ is the capacitance of the Helmholtz double layer, $E$ is the applied potential, $A$ is the sample area, $\varepsilon$ is the dielectric constant of the passive film, $\varepsilon_0$ is the vacuum permittivity ($8.854 \times 10^{-12}$ F.m$^{-1}$), $e$ is the electron charge, $N_{(d\ or\ A)}$ is the number of the donor or acceptor defects, $E_{fb}$ is the flat band potential, and $k$ and $T$ are Boltzmann constant and the absolute temperature, respectively. As the dielectric constant of a material is dependent on its chemical composition, passive layers with different chemical composition will have different dielectric constants. However, determining the exact dielectric constant for a thin layer is not trivial. Therefore, we have used a constant $\varepsilon$ in our calculations ($\varepsilon$=12) according to Hakiki et al. [38]. In the potential range of -0.6 to -0.4 V vs. SCE (i.e. flat bond potential) the capacitance of the Helmholtz double layer is ~44-55 µF.cm$^{-2}$, consistent with earlier studies [39]. For highly doped semiconductors, a significant part of the potential difference at the semiconductor/electrolyte interface extends to the Helmholtz layer in the solution and therefore the $C_H$ contribution should not be neglected [40-43]. Furthermore, due to the high density of the defects in the passive layer (*vide infra)*, voltage dependence of the film thickness, and the effect of surface states and adsorption events, Mott-Schottky EIS analysis can only serve as a semi-quantitative method [23]. In Fig. 1e we have plotted $C^{-2}$ against E. A positive slope in this plot indicates an n-type charge carrier behavior, whereas the opposite reflects a p-type semi-conductor [1, 44]. As is depicted in Fig. 1e, the charge carrier property of the passive film on super DSS transforms from a p-type semi-conductor (region I) to an n-type semiconductor (region II) when the potential passes -0.5 V vs. SCE. As will be discussed in the following, the passive layers with

p-type and n-type characteristics correspond to the inner and outer layers of the passive film, respectively, which is in agreement with the earlier studies on similar systems [42, 43, 45-48]. Between 0.3 V and 0.8 V vs. SCE (region III), the p-type behavior of the passive film is probably due to the increased concentration of the cation vacancies [23]. Beyond 0.8 V vs. SCE (region IV), the passive layer shows an n-type behavior due to the dissolution of chromium oxide. At this potential range, iron is the dominating component of the barrier film [23]. Changes in the semi-conducting characteristics of the passive layer from p-type to n-type (i.e. region I to II) are accompanied by a slight decrease in the number of defects (from $N_a = 23.10^{20}$ $cm^{-3}$ to $N_d = 20.10^{20}$ $cm^{-3}$).

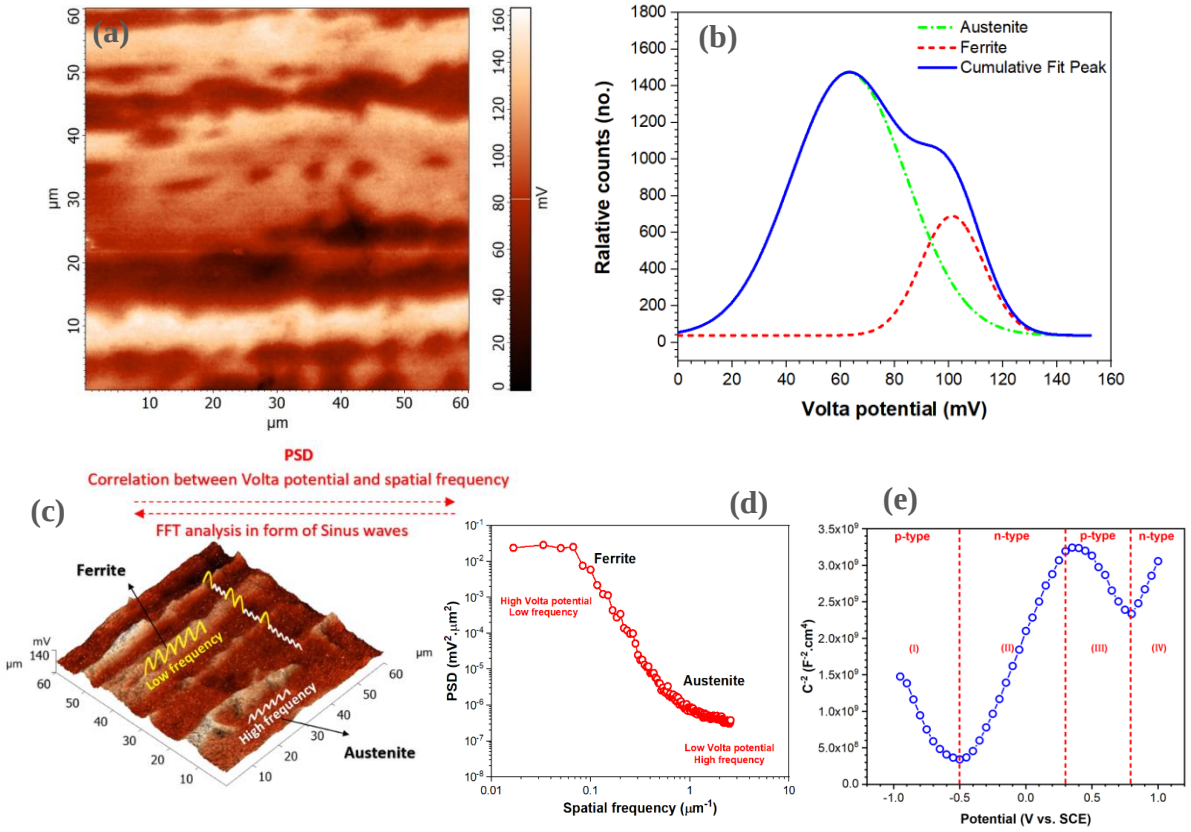


**Figure 1**. (a) Volta potential distribution over austenite and ferrite phases in super DSS, (b) Histogram representation of the Volta potential distribution, (c) Schematic depiction of correlation between the Volta potential distribution and spatial frequency for surface constituents, (d) PSD profile of the Volta potential distribution on super DSS sample, (e) Mott-Schottky EIS analysis of super DSS sample in the 3.5% NaCl corrosive solution.

Lanuzzi et al., suggested that tungsten containing DSS in contact with a saline solution directly forms $WO_3$, which is responsible for the improved localized corrosion resistance of DSS [9]. Furthermore, tungsten promotes the stability of molybdenum, chromium, and iron and consequently contributes to the stability of the passive film [10].

Since the content of alloying elements within coexisting ferrite and austenite phases is different (Table 1), the passive layers on individual phases are expected to possess dissimilar chemical compositions. To assess this presumption, (S)TEM/EDS examinations were carried out to microstructurally and chemically characterize the passive films grown on austenite and ferrite phases. Fig. 2a shows a high angle annular dark filed STEM (HAADF-STEM) image of the passive film around a ferrite/austenite interface. The inset in Fig. 2 (zoomed-in image) clearly shows the contrast between the bulk and oxide passive layer. No variation in passive layers thickness is observed, despite the fact that a thicker layer of passive film is expected generally to form on ferrite phase [11]. Nevertheless, galvanic activities between ferrite and austenite in a chloride-free solution might accelerate the growth of the passive film on austenite, whereby an identical thickness of both phases is oxidized. According to the HAADF-STEM image, the passive layer thickness is approximately 6.5 nm. Fig. 2b and c show the high resolution TEM images of austenite (left) and ferrite (right) phases. The atomic arrangement of crystalline bulk ferrite and austenite phases in these figures is noticeably distinguishable from the fully amorphous passive layer. In contrast, Zhang et al. observed partially crystalline structure or nano crystals at the interface between the bulk phase and the passive layer [4].

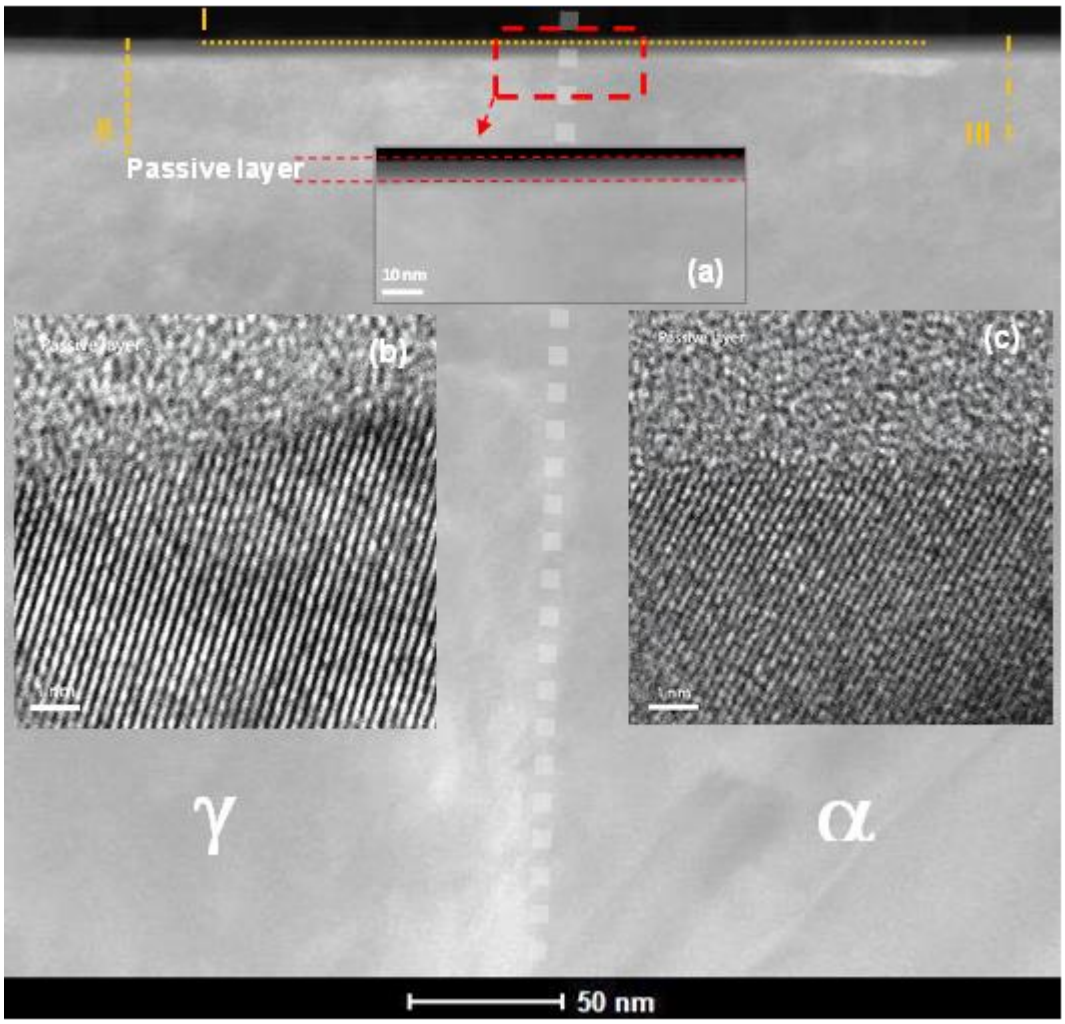


**Figure 2**. (a) HAADF-STEM image showing austenite and ferrite phase. The specimen was fabricated using FIB and lift-out technique around the austenite/ferrite grain boundary region. The passive layer is formed by immersing a mirror-like polished bulk sample in 45% $HNO_3$ solution for 24 h. Inset a shows a zoomed-in image of the sample with a passive layer of ca. 6.5 nm thick on top; interestingly no thickness variation is observed comparatively over austenite and ferrite. (b) and (c) show high resolution TEM images of austenite (left) and ferrite (right) phase. The amorphous passive layer is readily distinguishable from the crystalline bulk.

Fig. 3a represents the STEM image and EDS mapping results along the austenite/ferrite boundary on super DSS. The EDS elemental maps demonstrate the higher content of nickel and nitrogen in the austenite phase and higher amount of chromium, molybdenum, and tungsten in ferrite (phase stabilizer) [9, 13]. It is worth noting however, as was mentioned earlier, the effect of passive layer formation condition on the distribution of the alloying elements should not be neglected [24]. To

better demonstrate the distribution of tungsten and molybdenum within the passive layer, their EDS maps were superimposed on the STEM image, as shown in Fig. 3b. This figure clearly shows that molybdenum is rather distributed within the inner passive layer whereas tungsten is spread over the whole layer. EDS line profile in Fig. 3c reveals the elemental distribution within the passive film along the austenite/ferrite interface (denoted with line I in Fig. 2). Comparing the EDS maps in Fig. 3a and the elemental profile along line I, a qualitative correlation can be drawn; the alloying elements are incorporated into the passive layer depending on their levels in the bulk state. Nevertheless, the content ratio of alloying elements in bulk and in the passive layer of the corresponding phase is clearly different.

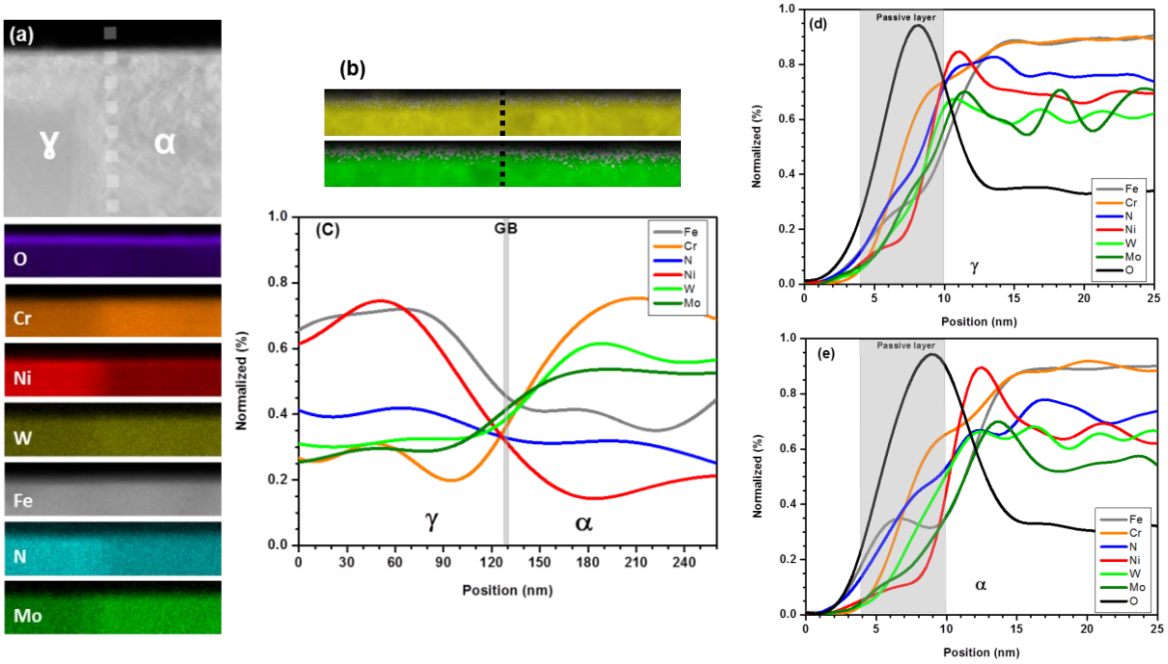


**Figure 3**. (a) STEM image and EDS elemental maps, showing the distribution of alloying elements in austenite and ferrite. (b) Tungsten (top) and molybdenum (bottom) map superimposed on the STEM image to better show the element distribution within the passive layer. (c) Distribution of alloying elements in the passive film across the austenite/ferrite boundary (marked with line I in Fig. 2). The composition of passive layer is distinctly different from that in the bulk for both ferrite and austenite phases (Table 1). Cross sectional elemental profiles in (d) austenite (along line II in Fig. 2) and (e) ferrite (along line II in Fig. 2). As the border between the inner and outer passive layer is not sharp, the schematically shown passive layer is not divided into two sections.

Elemental depth profiles in Fig. 3d and e demonstrate the elemental distribution in the passive film from surface towards bulk along the line II and line III in Fig. 2, respectively. In the case of austenite phase, the alloying elements are mainly accommodated within the inner part of the passive film. Specifically, nickel has accumulated in the matrix, close to the passive film, where a slight chromium depletion is detectable. Interestingly, nitrogen is also found within the entire passive layer. An enrichment of iron in the outer part of the passive film is clearly observed in ferrite phase, a phenomenon which is less pronounced in austenite phase. The distribution pattern of chromium, tungsten, molybdenum, and nickel seems to be similar to that in the austenite phase. The passive layers on austenite and ferrite phases can be divided into inner and outer regions accordingly. This is in conformity with the Mott-Schottky EIS results from which different semi-conductive properties for inner and outer parts of the passive layer were discussed. The results unravel that the local composition brings about different charge carrier properties. Overall, based on the elemental distribution within the passive layer, the formation of chromium oxides/nitrides in the inner passive layer with p-type semiconducting characteristics is plausible. Nitrogen presence in the outer layer might lead to the formation of iron and tungsten oxides/nitrides, which possibly provide self-healing properties for the passive layer as recently proposed procedure by Wang et al [49].

Based on the earlier Mott-Schottky EIS results and EDS analysis on individual phases, we conclude that the p-type behavior in the inner part of passive film, which is related to more and effective presence of tungsten and molybdenum in this region, is more pronounced for the ferrite phase compared to that for austenite phase. These observations can also explain the improved integrity of the passive film on this phase, as reported in the previous study [9, 21].

To further correlate relative Volta potential, $N_a$ and $N_d$ in Mott-Schottky EIS, and chemical composition of individual phases on super DSS, we conducted complementary STS measurements. In STS analysis, a bias voltage is applied between a conductive tip and the sample surface to generate a tunneling current flowing across a potential barrier [28]. When the tunneling gap between the tip and the sample surface is small and the applied bias voltage is low, the correlation of the tunneling current (I) to the gap distance (S) can be defined as follows [50]:

$$I \propto \frac{V}{S} e^{-A\Phi^{1/2}S} \quad (4)$$

where $\Phi$ is the work function, $V$ is applied bias voltage, and constant $A$ equals 1.025 $(eV)^{-1/2}$. Mechehoud et al. showed that the band gap values measured by STS are comparable to those extracted from photoelectrochemical evaluations [51]. For a constant S, the total tunneling current has a direct correlation with the number of surface defects on the sample surface [52, 53]. Therefore, the dI/dV vs. V curve can be used as a representative for the local semi-conductive characteristic of the passive film on individual phases. As aforementioned, the passive films on ferrite and austenite phases have different chemical compositions and consequently dissimilar work functions. To further evaluate this phenomenon, the dI/dV vs. V curves for austenite and ferrite are provided in Fig. 4a and b, respectively. In these figures, the local conduction band potential ($E_c$) and local valence band potential ($E_v$) can be determined by selection of the first sharp rise of dI/dV where the negative and positive values represent, in their respected order, the occupied and unoccupied electron density states [53]. Therefore, $\Delta V$ ($E_c$-$E_v$) can be correlated to the local surface electronic gap energy ($E_g$) of the corresponding passive films. Fig. 4 demonstrates that the ferrite phase has a larger local surface electronic gap energy ($E_g$ ~ 0.46 eV) than austenite phase ($E_g$ ~ 0.20 eV). The higher $E_g$ on ferrite phase in comparison with that on the austenite is attributed generally to the positive role of chromium and molybdenum [7]. Furthermore, the presence of tungsten can promote the stability of the passive film. It has been shown, by Marcus et al [53] and Greiner et al [54], that the global band gap energy of $WO_3$, with n-type semi-conductor character and cubic simple structure, is in the range of 2.5 to 3.2 eV. Nevertheless, due to the local sensitivity and defects influence, the local band gap potentials values measured by STS are lower than the global band gaps which are reported for bulk oxides [52]. Based on the EDS profiles formation of other tungsten oxides and more specifically the tungsten nitrides is also expected in the passive layer, on both phases. Formation of these oxides also affects the band gap energy in the passive layer. Based on our results, the impact of tungsten on modification of the semi-conductive properties (expected to improve corrosion resistance) of the passive film is more pronounced for the ferrite phase.

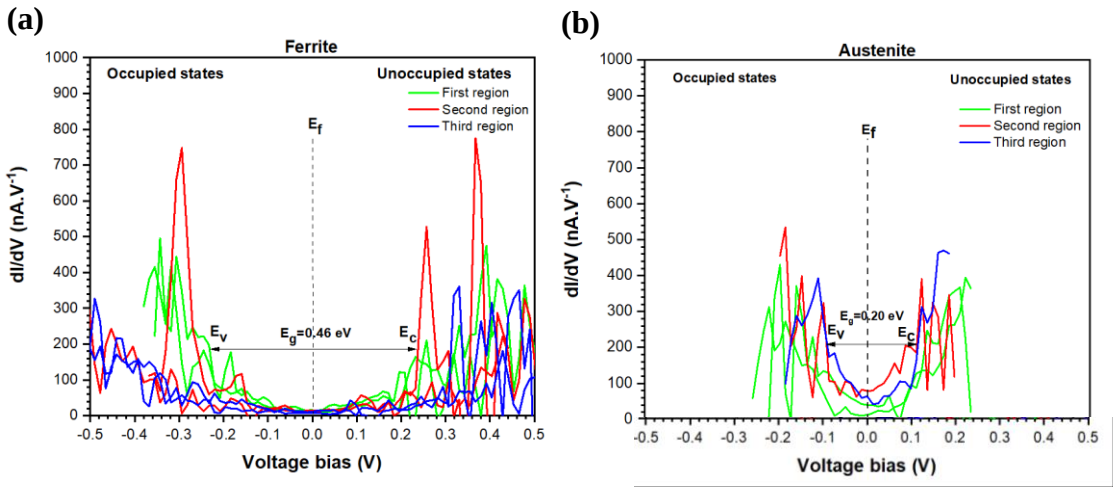


**Figure 4**. STS results showing the differential conductance spectra (dI/dV vs. V) on (a) ferrite and (b) austenite phases. All the experiments were performed on air-formed passive film at 27 ºC and relative humidity of 28% ± 1. For better counting statistics, multiple STS measurements were performed on each phase and different colors represent different runs.

Overall, the results obtained in the present study (SKPFM, STEM-EDS and STS) indicate that tungsten is enhancing passive layer integrity on ferrite phase whereas the austenite still needs improvement, by adding other effective alloying elements, in terms of corrosion properties. The synergy between additional alloying elements in this regard is also an important factor. As previously observed by Olsson [55], nitrogen and molybdenum interaction near the passive layer region in DSS enhances the protective properties of the passive layer, independent of the underlying phase. Similarly, Kim et al. investigated the synergism between iron dissolution and molybdenum formation due to the substitution of tungsten in SS [10]. The beneficial effect of tungsten on the pitting and crevice corrosion resistance of DSS was further assessed by Haugan et al. [9]. Furtheremore, Liou et al. systematically explored the synergistic effect of alloying elements on the cracking sensitivity and ductility of DSS [56]. According to these studies, in the design of DSS alloys with improved corrosion or mechanical properties, the synergistic effect of additional alloying elements should also be considered. Although designing the alloys for specific corrosion or mechanical performance is beyond the scopes of this manuscript, a thorough characterization of the passive layers on individual phases, such as the research performed in this study, is crucial for exploration of the synergistic effects of the alloying elements on the overall performance of the alloy. Besides, assessing the impact of passive layers with different properties on individual phases

in DSS on their corrosion protection efficiency, requires further local electrochemical measurements which is ongoing in our groups.

## 4. Conclusions

A comprehensive study was conducted on a super DSS (S39274) in order to investigate the role of alloying elements in passive layer properties on individual ferrite and austenite phases. Mott-Schottky EIS analysis confirmed that the passive film on super DSS is composed of a p-type inner layer and an n-type outer layer. The contribution of tungsten and molybdenum, as minor alloying elements, to passive layer buildup was studied and their presence in the passive layer was directly evidenced by STEM/EDS analysis. A slight chromium depletion and considerable nickel accumulation was detected in the inner layer of the passive film at the metal/oxide interface. It was shown that the passive layer formed on the ferrite phase contains more molybdenum, tungsten, and chromium which provide ferrite with a higher nobility than the austenite phase. Finally, the STS examinations measured higher local energy of the band gap for the air-formed passive layer on ferrite compared to that on the austenite phase. A combination of the findings herein can be used to explain dissimilar corrosion properties of the austenite and ferrite in super DSS (S39274).

## Acknowledgement

Ferdowsi University of Mashhad, Hakim Sabzevari University and Delft University of Technology are appreciated for providing SKPFM, STS, Mott-Schottky EIS, and STEM setups. A. Rafsanjani and A. Imani are acknowldge for conducting the STS and SKPFM measurements. The TEM work is supported by Nederlandse Organisatie voor Wetenschappelijk Onderzoek (NWO) under project number UPON B2 14205. SH thanks Prof. W. Peukert and Emerging Talents Initiative (ETI) 2018/2_Tech_06, FAU, Germany grant for supporting his research.

**References:**

[1] X. Cheng, Y. Wang, C. Dong, X. Li, The beneficial galvanic effect of the constituent phases in 2205 duplex stainless steel on the passive films formed in a 3.5% NaCl solution, Corrosion Science, 134 (2018) 122.
[2] Y. Wang, X. Cheng, X. Li, Electrochemical behavior and compositions of passive films formed on the constituent phases of duplex stainless steel without coupling, Electrochemistry Communications, 57 (2015) 56.
[3] E. Hamada, K. Yamada, M. Nagoshi, N. Makiishi, K. Sato, T. Ishii, K. Fukuda, S. Ishikawa, T. Ujiro, Direct imaging of native passive film on stainless steel by aberration corrected STEM, Corrosion Science, 52 (2010) 3851.
[4] B. Zhang, J. Wang, B. Wu, X.W. Guo, Y.J. Wang, D. Chen, Y.C. Zhang, K. Du, E.E. Oguzie, X.L. Ma, Unmasking chloride attack on the passive film of metals, Nature Communications, 9 (2018) 2559.
[5] W.-T. Tsai, J.-R. Chen, Galvanic corrosion between the constituent phases in duplex stainless steel, Corrosion Science, 49 (2007) 3659.
[6] M. Långberg, C. Örnek, J. Evertsson, G.S. Harlow, W. Linpé, L. Rullik, F. Carlà, R. Felici, E. Bettini, U. Kivisäkk, E. Lundgren, J. Pan, Redefining passivity breakdown of super duplex stainless steel by electrochemical operando synchrotron near surface X-ray analyses, npj Materials Degradation, 3 (2019) 22.
[7] L.Q. Guo, M.C. Lin, L.J. Qiao, A.A. Volinsky, Duplex stainless steel passive film electrical properties studied by in situ current sensing atomic force microscopy, Corrosion Science, 78 (2014) 55.
[8] T. Souier, F. Martin, C. Bataillon, J. Cousty, Local electrical characteristics of passive films formed on stainless steel surfaces by current sensing atomic force microscopy, Applied Surface Science, 256 (2010) 2434.
[9] E.B. Haugan, M. Næss, C.T. Rodriguez, R. Johnsen, M. Iannuzzi, Effect of Tungsten on the Pitting and Crevice Corrosion Resistance of Type 25Cr Super Duplex Stainless Steels, Corrosion, 73 (2017) 53.
[10] J.S. Kim, P.J. Xiang, K.Y. Kim, Effect of Tungsten and Nickel Addition on the Repassivation Behavior of Stainless Steel, Corrosion, 61 (2005) 174.
[11] B. Zhang, X.X. Wei, B. Wu, J. Wang, X.H. Shao, L.X. Yang, S.J. Zheng, Y.T. Zhou, Q.Q. Jin, E.E. Oguzie, X.L. Ma, Chloride attack on the passive film of duplex alloy, Corrosion Science, (2019) 123.
[12] M. Femenia, J. Pan, C. Leygraf, In Situ Local Dissolution of Duplex Stainless Steels in 1 M $H_2SO_4$ + 1 M NaCl by Electrochemical Scanning Tunneling Microscopy, Journal of The Electrochemical Society, 149 (2002) B187.
[13] M. Femenia, J. Pan, C. Leygraf, Characterization of Ferrite-Austenite Boundary Region of Duplex Stainless Steels by SAES, Journal of The Electrochemical Society, 151 (2004) B581.
[14] L. Guo, G. Hua, B. Yang, H. Lu, L. Qiao, X. Yan, D. Li, Electron work functions of ferrite and austenite phases in a duplex stainless steel and their adhesive forces with AFM silicon probe, Scientific Reports, 6 (2016) 20660.
[15] M. Rohwerder, F. Turcu, High-resolution Kelvin probe microscopy in corrosion science: Scanning Kelvin probe force microscopy (SKPFM) versus classical scanning Kelvin probe (SKP), Electrochimica Acta, 53 (2007) 290.
[16] L.Q. Guo, M.C. Lin, L.J. Qiao, A.A. Volinsky, Ferrite and austenite phase identification in duplex stainless steel using SPM techniques, Applied Surface Science, 287 (2013) 499.

[17] K.S.d. Assis, F.V.V.d. Sousa, M. Miranda, I.C.P. Margarit-Mattos, V. Vivier, O.R. Mattos, Assessment of electrochemical methods used on corrosion of superduplex stainless steel, Corrosion Science, 59 (2012) 71.
[18] Y. Jin, Z. Lai, P. Bi, S. Yan, L. Wen, Y. Wang, J. Pan, C. Leygraf, Combining lithography and capillary techniques for local electrochemical property measurements, Electrochemistry Communications, 87 (2018) 53.
[19] C. Örnek, J. Walton, T. Hashimoto, T.L. Ladwein, S.B. Lyon, D.L. Engelberg, Characterization of 475°C Embrittlement of Duplex Stainless Steel Microstructure via Scanning Kelvin Probe Force Microscopy and Magnetic Force Microscopy, Journal of The Electrochemical Society, 164 (2017) C207.
[20] N. Sathirachinda, R. Pettersson, J. Pan, Depletion effects at phase boundaries in 2205 duplex stainless steel characterized with SKPFM and TEM/EDS, Corrosion Science, 51 (2009) 1850.
[21] C. Örnek, D.L. Engelberg, SKPFM measured Volta potential correlated with strain localisation in microstructure to understand corrosion susceptibility of cold-rolled grade 2205 duplex stainless steel, Corrosion Science, 99 (2015) 164.
[22] M. Li, L.Q. Guo, L.J. Qiao, Y. Bai, The mechanism of hydrogen-induced pitting corrosion in duplex stainless steel studied by SKPFM, Corrosion Science, 60 (2012) 76.
[23] J. Yao, D.d. Macdonald, C. Dong, Passive film on 2205 duplex stainless steel studied by photo-electrochemistry and ARXPS methods, Corrosion Science, 146 (2019) 221.
[24] E. Gardin, S. Zanna, A. Seyeux, A. Allion-Maurer, P. Marcus, XPS and ToF-SIMS characterization of the surface oxides on lean duplex stainless steel – Global and local approaches, Corrosion Science, (2019) 121.
[25] v. Guillaumin, P. Schmutz, G.S. Frankel, Characterization of Corrosion Interfaces by the Scanning Kelvin Probe Force Microscopy Technique, Journal of The Electrochemical Society, 148 (2001) B163.
[26] M. Iannuzzi, K.L. Vasanth, G.S. Frankel, Unusual Correlation between SKPFM and Corrosion of Nickel Aluminum Bronzes, Journal of The Electrochemical Society, 164 (2017) C488.
[27] E. Rahimi, A. Rafsanjani-Abbasi, A. Imani, S. Hosseinpour, A. Davoodi, Insights into Galvanic Corrosion Behavior of Ti-Cu Dissimilar Joint: Effect of Microstructure and Volta Potential, Materials (Basel, Switzerland), 11 (2018) 1820.
[28] E. Rahimi, A. Rafsanjani-Abbasi, A. Imani, S. Hosseinpour, A. Davoodi, Correlation of surface Volta potential with galvanic corrosion initiation sites in solid-state welded Ti-Cu bimetal using AFM-SKPFM, Corrosion Science, 140 (2018) 30.
[29] A. International, ASTM E1086-14, in: Standard Test Method for Analysis of Austenitic Stainless Steel by Spark Atomic Emission Spectrometry, West Conshohocken, PA, 2014.
[30] A. International, ASTM E3-11 in: Standard Guide for Preparation of Metallographic Specimens, West Conshohocken, PA, 2017.
[31] V.A. Valencia, A.A. Thaker, J. Derouin, D.N. Valencia, R.G. Farber, D.A. Gebel, D.R. Killelea, Preparation of scanning tunneling microscopy tips using pulsed alternating current etching, Journal of Vacuum Science & Technology A: Vacuum, Surfaces, and Films, 33 (2015) 023001.
[32] L.A. Giannuzzi, F.A. Stevie, Introduction to focused ion beams: Instrumentation, theory, techniques, and practice / edited by Lucille A. Giannuzzi, Fred A. Stevie, in, Springer, New York, 2004.
[33] H.B. Michaelson, The work function of the elements and its periodicity, Journal of Applied Physics, 48 (1977) 4729.

[34] Z. Esfahani, E. Rahimi, M. Sarvghad, A. Rafsanjani-Abbasi, A. Davoodi, Correlation between the histogram and power spectral density analysis of AFM and SKPFM images in an AA7023/AA5083 FSW joint, Journal of Alloys and Compounds, 744 (2018) 174.
[35] X.-x. Yu, A. Gulec, Q. Sherman, K.L. Cwalina, J.R. Scully, J.H. Perepezko, P.W. Voorhees, L.D. Marks, Nonequilibrium Solute Capture in Passivating Oxide Films, Physical Review Letters, 121 (2018) 145701.
[36] M. Flemming, L. Coriand, A. Duparré, Ultra-hydrophobicity Through Stochastic Surface Roughness, Journal of Adhesion Science and Technology, 23 (2009) 381.
[37] N.F. Mott, The theory of crystal rectifiers, Proceedings of the Royal Society of London. Series A. Mathematical and Physical Sciences, 171 (1939) 27.
[38] N.E. Hakiki, M. Da Cunha Belo, A.M.P. Simões, M.G.S. Ferreira, Semiconducting Properties of Passive Films Formed on Stainless Steels: Influence of the Alloying Elements, Journal of The Electrochemical Society, 145 (1998) 3821.
[39] M.E. Orazem, B. Tribollet, Electrochemical impedance spectroscopy, John Wiley & Sons, 2017.
[40] J.O.M. Bockris, K. Uosaki, H. Kita, Interfacial electron transfer as a significant step in photoelectrochemical reactions on some semiconductors, Journal of Applied Physics, 52 (1981) 808.
[41] K. Uosaki, H. Kita, Effects of the Helmholtz Layer Capacitance on the Potential Distribution at Semiconductor/Electrolyte Interface and the Linearity of the Mott-Schottky Plot, Journal of The Electrochemical Society, 130 (1983) 895.
[42] N.B. Hakiki, S. Boudin, B. Rondot, M. Da Cunha Belo, The electronic structure of passive films formed on stainless steels, Corrosion Science, 37 (1995) 1809.
[43] R.M. Fernández-Domene, E. Blasco-Tamarit, D.M. García-García, J. García-Antón, Passive and transpassive behaviour of Alloy 31 in a heavy brine LiBr solution, Electrochimica Acta, 95 (2013) 1.
[44] Z. Feng, X. Cheng, C. Dong, L. Xu, X. Li, Passivity of 316L stainless steel in borate buffer solution studied by Mott–Schottky analysis, atomic absorption spectrometry and X-ray photoelectron spectroscopy, Corrosion Science, 52 (2010) 3646.
[45] H. Tsuchiya, S. Fujimoto, O. Chihara, T. Shibata, Semiconductive behavior of passive films formed on pure Cr and Fe–Cr alloys in sulfuric acid solution, Electrochimica Acta, 47 (2002) 4357.
[46] A.C. Lloyd, J.J. Noël, S. McIntyre, D.W. Shoesmith, Cr, Mo and W alloying additions in Ni and their effect on passivity, Electrochimica Acta, 49 (2004) 3015.
[47] H. Luo, C.F. Dong, X.G. Li, K. Xiao, The electrochemical behaviour of 2205 duplex stainless steel in alkaline solutions with different pH in the presence of chloride, Electrochimica Acta, 64 (2012) 211.
[48] R.M. Fernández-Domene, E. Blasco-Tamarit, D.M. García-García, J. García-Antón, Effect of alloying elements on the electronic properties of thin passive films formed on carbon steel, ferritic and austenitic stainless steels in a highly concentrated LiBr solution, Thin Solid Films, 558 (2014) 252.
[49] Q. Wang, B. Zhang, Y. Ren, K. Yang, A self-healing stainless steel: Role of nitrogen in eliminating detrimental effect of cold working on pitting corrosion resistance, Corrosion Science, 145 (2018) 55.
[50] T. Knutsen, S. Diplas, T. Våland, S. Jørgensen, T. Norby, A Study of Anodically Grown Hydroxide Films on an Amorphous Ni[sub 78]Si[sub 8]B[sub 14] Alloy, Journal of The Electrochemical Society, 154 (2007) F111.

[51] F. Mechehoud, N.E. Benaioun, N.E. Hakiki, A. Khelil, L. Simon, J.L. Bubendorff, Thermally oxidized Inconel 600 and 690 nickel-based alloys characterizations by combination of global photoelectrochemistry and local near-field microscopy techniques (STM, STS, AFM, SKPFM), Applied Surface Science, 433 (2018) 66.
[52] V. Maurice, P. Marcus, Current developments of nanoscale insight into corrosion protection by passive oxide films, Current Opinion in Solid State and Materials Science, 22 (2018) 156.
[53] P. Marcus, V. Maurice, Atomic level characterization in corrosion studies, Philosophical transactions. Series A, Mathematical, physical, and engineering sciences, 375 (2017) 20160414.
[54] M.T. Greiner, M.G. Helander, W.-M. Tang, Z.-B. Wang, J. Qiu, Z.-H. Lu, Universal energy-level alignment of molecules on metal oxides, Nature Materials, 11 (2011) 76.
[55] C.-O.A. Olsson, The influence of nitrogen and molybdenum on passive films formed on the austenoferritic stainless steel 2205 studied by AES and XPS, Corrosion Science, 37 (1995) 467.
[56] H.-Y. Liou, W.-T. Tsai, Y.-T. Pan, R.-I. Hsieh, Effects of alloying elements on the mechanical properties and corrosion behaviors of 2205 duplex stainless steels, Journal of Materials Engineering and Performance, 10 (2001) 231.